



<b>Publication Year</b>	2021
<b>Acceptance in OA @INAF</b>	2023-01-26T13:02:09Z
<b>Title</b>	Thermal inertia of Occator's faculae on Ceres
<b>Authors</b>	Rognini, E.; CAPRIA, MARIA TERESA; TOSI, Federico; DE SANCTIS, MARIA CRISTINA; Ciarniello, M.; et al.
<b>DOI</b>	10.1016/j.pss.2021.105285
<b>Handle</b>	<a href="http://hdl.handle.net/20.500.12386/33081">http://hdl.handle.net/20.500.12386/33081</a>
<b>Journal</b>	PLANETARY AND SPACE SCIENCE
<b>Number</b>	205

# Journal Pre-proof



Thermal inertia of Occator's faculae on Ceres

E. Rognini, M.T. Capria, F. Tosi, M.C. De Sanctis, M. Ciarniello, A. Longobardo, F.G. Carrozzo, A. Raponi, M. Formisano, A. Frigeri, E. Palomba, S. Fonte, M. Giardino, E. Ammannito, C.A. Raymond, C.T. Russell

PII: S0032-0633(21)00124-0

DOI: <https://doi.org/10.1016/j.pss.2021.105285>

Reference: PSS 105285

To appear in: *Planetary and Space Science*

Received Date: 30 January 2020

Revised Date: 9 June 2021

Accepted Date: 13 June 2021

Please cite this article as: Rognini, E., Capria, M.T., Tosi, F., De Sanctis, M.C., Ciarniello, M., Longobardo, A., Carrozzo, F.G., Raponi, A., Formisano, M., Frigeri, A., Palomba, E., Fonte, S., Giardino, M., Ammannito, E., Raymond, C.A., Russell, C.T., Thermal inertia of Occator's faculae on Ceres, *Planetary and Space Science*, <https://doi.org/10.1016/j.pss.2021.105285>.

This is a PDF file of an article that has undergone enhancements after acceptance, such as the addition of a cover page and metadata, and formatting for readability, but it is not yet the definitive version of record. This version will undergo additional copyediting, typesetting and review before it is published in its final form, but we are providing this version to give early visibility of the article. Please note that, during the production process, errors may be discovered which could affect the content, and all legal disclaimers that apply to the journal pertain.

© 2021 Published by Elsevier Ltd.

## **CRediT author statement**

Edoardo Rognini: Software, Writing – original draft, Formal analysis

Maria Teresa Capria: Software, Formal analysis

Federico Tosi: Formal analysis

Maria Cristina De Sanctis: Writing - Review & Editing

Mauro Ciarniello: Writing - Review & Editing

Andrea Longobardo: Writing - Review & Editing

Giacomo Carrozzo: Writing - Review & Editing

Andrea Raponi: Writing - Review & Editing

Michelangelo Formisano: Writing - Review & Editing

Alessandro Frigeri: Writing - Review & Editing

Ernesto Palomba: Writing - Review & Editing

Sergio Fonte: Writing - Review & Editing, Data Curation

Marco Giardino: Writing - Review & Editing , Data Curation

Eleonora Ammannito: Writing - Review & Editing

Carol Raymond: Writing - Review & Editing

Christopher Russell: Writing - Review & Editing

## Thermal inertia of Occator's faculae on Ceres

1  
2  
3  
4  
5  
6  
7  
8  
9  
10  
11  
12  
13  
14  
15  
16  
17  
18  
19  
20  
21  
22

**E. Rognini**<sup>1,2</sup>, M. T. Capria<sup>3</sup>, F. Tosi<sup>3</sup>, M. C. De Sanctis<sup>3</sup>, M. Ciarniello<sup>3</sup>, A. Longobardo<sup>3,4</sup>,  
F. G. Carrozzo<sup>3</sup>, A. Raponi<sup>3</sup>, M. Formisano<sup>3</sup>, A. Frigeri<sup>3</sup>, E. Palomba<sup>3</sup>, S. Fonte<sup>3</sup>, M.  
Giardino<sup>1</sup>, E. Ammannito<sup>5</sup>, C. A. Raymond<sup>6</sup>, C. T. Russell<sup>7</sup>

**Corresponding author:** Edoardo Rognini, ASI-SSDC, via del Politecnico snc, I-00133 Rome ,  
Italy. E-mail: *edoardo.rognini@ssdc.asi.it*

<sup>1</sup> ASI Space Science Data Center (SSDC), Via del Politecnico snc, 00133 Rome, Italy

<sup>2</sup> INAF-OAR Osservatorio Astronomico di Roma, Via Frascati 33, 00040, Monte Porzio Catone  
(RM), Italy

<sup>3</sup> INAF-IAPS Istituto di Astrofisica e Planetologia Spaziali, Via del Fosso del Cavaliere 100, 00133  
Rome, Italy

<sup>4</sup> Università Parthenope, DIST, Centro Direzionale Isola C4, I-80143, Napoli, Italy

<sup>5</sup> Agenzia Spaziale Italiana, Via del Politecnico snc, 00133 Rome, Italy

<sup>6</sup> NASA/Jet Propulsion Laboratory and California Institute of Technology, Pasadena, CA, USA

<sup>7</sup> University of California at Los Angeles (UCLA), 90095 Los Angeles, CA, USA

### Key points

- The thermal inertia of Occator's faculae on Ceres has been derived using spatially resolved, high resolution VIR data from the Dawn mission.
- In the central part of the Cerealia facula a higher thermal inertia (up to about  $60 \text{ Jm}^{-2} \text{ s}^{-1/2} \text{ K}^{-1}$ ) with respect to the surrounding regions, corresponding to a thermal anomaly, has been derived.

## 23 Abstract

24 Thermal inertia is a key information to quantify the physical status of a planetary surface; it can be  
25 retrieved by comparison between theoretical and observed temperature diurnal profiles. We have  
26 calculated the surface temperature for a set of locations on Ceres' surface with a thermophysical  
27 model that provides temperature as a function of thermal conductivity and roughness, and we have  
28 determined the values of those parameters for which the best fit with the observed data is obtained.  
29 The observed temperatures have been retrieved from spatially-resolved data from the Dawn  
30 mission. In our previous work [Rognini *et al.*, 2019], we have found that the average thermal inertia  
31 for the overall surface of Ceres is low (from 1-15 to  $60 \text{ J m}^{-2} \text{ s}^{-1/2} \text{ K}^{-1}$ ), as expected according to the  
32 general trend observed in the Solar System for atmosphere-less bodies, while the thermal inertia of  
33 the very bright faculae found in the floor of the Occator crater could not be well defined. Using  
34 more recently acquired VIR high resolution data we find that the central part of the Cerealia facula  
35 displays a thermal anomaly ( $\sim 10 \text{ K}$  above the average) compatible with a higher thermal inertia  
36 with respect to the surrounding regions, while the Vinalia facula does not display any consequently  
37 could have a grain size comparable with the Ceres' surface average.

38 **Keywords:** thermal inertia, thermophysical model, Ceres, facula

## 39 1. Introduction and background

40 The dwarf planet Ceres is the largest and most massive body in the Main Asteroid Belt. Its size  
41 (mean diameter 939 km) suggests that it has experienced many of the processes typical of planet  
42 formation and evolution; its planet-like nature and its survival from the early stages of the Solar  
43 System make it an important object for understanding the planetary evolution.

44 The NASA Dawn mission [Russell *et al.*, 2011] was launched in 2007 with the goal of studying  
45 Vesta and Ceres, two of the largest bodies of the Main Belt. The Visible and InfraRed (VIR)

46 mapping spectrometer [De Sanctis et al., 2011] onboard the Dawn spacecraft operates in the overall  
 47 spectral range 0.25-5.1  $\mu\text{m}$ , with an Instantaneous Field of View (IFOV) of 250  $\mu\text{rad}/\text{pixel}$ , and a  
 48 spectral sampling of 1.8 nm/band in the 0.25-1.0 visual range and 9.8 nm/band in the 1-5  $\mu\text{m}$   
 49 infrared range. VIR was designed to provide mineralogical mapping of Vesta and Ceres. Its data are  
 50 stored as hyperspectral images or “cubes”, i.e. bidimensional images of the surface at varying  
 51 wavelength.

52 Dawn began orbiting Ceres in March 2015. This phase of the mission was divided in different sub-  
 53 phases, characterized by different altitudes and related VIR pixel resolution (**Tab. 1**): Rotational  
 54 Characterization orbit (RC3), Survey, High Altitude Mapping Orbit (HAMO), Low Altitude  
 55 Mapping Orbit (LAMO) for the nominal mission, plus Extended Mission phases 1 and 2 (XM1 and  
 56 XM2, with the second extended mission phase following an elliptical orbit). While the primary  
 57 scientific objective of VIR was to determine and map the surface mineralogy, the long-wavelength  
 58 component of the infrared spectra in the range  $4.5 \mu\text{m} < \lambda < 5.1 \mu\text{m}$  can be used to retrieve the  
 59 surface temperature; the retrieval is applied separately on each pixel unaffected by detector  
 60 saturation. The VIR instrument can sense temperatures within the uppermost surface layer as thick  
 61 as tens of microns; in the sampled spectral range the temperature is a non-linear function of  
 62 radiance, with a larger weight of the hottest sub-pixel features, so the obtained value is  
 63 representative of the subpixel regions at higher temperatures modulated by their effective areas.  
 64 Temperature values retrieved in this way show an accuracy better than 3 K above 180 K, and better  
 65 than 1 K above 210 K, while values below 180 K have increasingly worse accuracy. The lower  
 66 limit of temperatures sensed by the instrument is dictated by the in-flight instrumental noise,  
 67 varying over time depending on a number of parameters, most notably the spectrometer's  
 68 temperature.

69 Thermal inertia is defined as:

70 
$$TI = \sqrt{k\rho c} \quad (\text{J m}^{-2} \text{s}^{-1/2} \text{K}^{-1}) \quad (1)$$

71 where  $k$  is the thermal conductivity,  $\rho$  the density and  $c$  the specific heat; it is a fundamental  
72 parameter that controls the surface temperature variations of atmosphere-less bodies, and measures  
73 the velocity of penetration of the thermal wave controlling the surface temperature. The daily  
74 temperature curve of an airless body (i.e., the profile of surface temperature of a given location as a  
75 function of the local solar time (LST)), from which thermal inertia can be estimated [e.g.,  
76 *Neugebauer et al.*, 1971; *Audouard et al.*, 2014; *Delbo et al.*, 2015]), is strongly dependent on the  
77 physical and thermal properties of the uppermost surface layer, as thick as few centimeters.  
78 Therefore, the derivation of thermal inertia provides an insight into the structure and physical  
79 properties of that surface, giving indications on the type (e.g., dust, regolith or rock) and the  
80 physical structure of the surface material [*Harris and Lagerros*, 2002].

81 In a previous work [*Rognini et al.*, 2019], we modeled VIR data acquired during the Survey and  
82 HAMO mission phases with an average spatial resolution of 1.1 km/pixel and 0.38 km/pixel,  
83 respectively. We derived the average thermal inertia of Ceres and of two specific locations: the  
84 crater Haulani and the crater Occator. The average thermal inertia of Ceres turned out to be  
85 relatively low ( $\sim 60 \text{ J m}^{-2} \text{ s}^{-1/2} \text{ K}^{-1}$ ), which confirms previous independent estimations and is  
86 compatible with the trend of the thermal inertia as function of diameter found for the airless bodies  
87 of the Main Asteroid Belt [*Delbo and Tanga*, 2008]. Crater Haulani revealed a higher than the  
88 average thermal inertia in its central mountainous ridge (up to 130-140  $\text{J m}^{-2} \text{ s}^{-1/2} \text{ K}^{-1}$ ),  
89 corresponding to the most distinct thermal signature on the entire surface of Ceres (Tosi et al.,  
90 2018a), which is probably due to the compactness of that particular geologic feature. Conversely,  
91 crater Occator, as seen at spatial resolution as high as 0.38 km/pixel, could hardly display any  
92 thermal signature, and its surface temperatures could be fitted by theoretical diurnal temperature  
93 profiles associated with a broad range of thermal inertia values.

94 In this work, we follow up our analysis on the bright spots (“faculae”) located in crater Occator by  
95 using VIR data acquired during the final, elliptical XM2 phase mission at much higher pixel

96 resolution (9-11 m/pixel). Occator is a 92-km wide crater, centered at 19.7°N 239.6°E. Occator's  
 97 facula cluster is formed by a very bright spot located in the center of the crater (*Cerealia Facula*),  
 98 and a secondary group of bright spots in the eastern floor, named *Vinalia Facula*. In particular,  
 99 *Cerealia Facula* is the brightest material unit on Ceres with an average visual normal albedo of  
 100 about 0.6 at a resolution of 1.3 km per pixel (several times Ceres's average) [Schröder *et al.*, 2017;  
 101 Longobardo *et al.*, 2017a]. The spectral slope indicates that the crater interior is younger than the  
 102 crater walls, and the white material of the faculae is likely even younger: age estimations give  $34 \pm$   
 103  $2$  Ma [Nathues *et al.*, 2015] for Occator and  $6.9 \pm 0.9$  Ma for the floor material [Nathues *et al.*,  
 104 2016]. Mass deposits originate from the wall of the crater and extend to the floor for 10-20 km, and  
 105 are covered, at SW and NE, by floor material that extends from the center. The features of these  
 106 morphological structures, the presence of fractures and their orientation and age, the central  
 107 depression all suggest post impact processes such as hydrothermal processes, evaporation and  
 108 emplacement of flow materials [Jaumann *et al.*, 2017]. The spectra of the faculae suggest a  
 109 composition of a mixture of anhydrous sodium carbonate or natrite ( $\text{Na}_2\text{CO}_3$ ) and ammonium  
 110 chloride ( $\text{NH}_4\text{Cl}$ ) or ammonium bicarbonate ( $\text{NH}_4\text{HCO}_3$ ) [Raponi *et al.*, 2019; De Sanctis *et al.*,  
 111 2016; Carozzo *et al.*, 2018; Palomba *et al.*, 2019]. The faculae probably originated from a  
 112 relatively recent crystallization of brines that made their way from a subsurface liquid reservoir up  
 113 to the surface [De Sanctis *et al.*, 2016; Stein *et al.*, 2017]. VIR data of the Occator crater acquired  
 114 on 11, 13, 23 and 24 June 2018, despite their sparse coverage and non-optimal signal-to-noise ratio,  
 115 first revealed that the central part of the *Cerealia* facula is about 10 K cooler than the surrounding  
 116 areas, while *Vinalia* facula has no thermal contrast compared to the rest of the eastern floor [Tosi *et*  
 117 *al.*, 2018b].

118

Mission phase	Starting date	End date	Altitude (km)	Pixel resolution (m)

RC3		April 23, 2015	May 9, 2015	13,522-13,637	3380-3409
SURVEY		June 6, 2015	June 30, 2015	4380-4423	1095-1106
HAMO		August 17, 2015	October 23, 2015	1450-1475	363-369
LAMO		December 16, 2015	September 2, 2016	355-403	89-101
XM1	XMO1	19 Jun 2016	2 Sep 2016	378	95
	XMO2	10 Oct 2016	04 Nov 2016	1522	380
	XMO3	21 Jan 2017	17 Feb 2017	7738	1930
	XMO4	29 Apr 2017	24 May 2017	19457	4860
XM2		May 21, 2018	July 15, 2018	29-2662	7-665

119 **Table 1.** Characteristics of the mission phases of Dawn around Ceres. Data from XM2, i.e. the last mission phase, have  
 120 been used in this work.

121

## 122 **2. Thermophysical analysis of the Occator faculae**

### 123 **2.1 Temperature retrieval method**

124 The method used to derive surface temperatures and spectral emissivity from VIR data is described  
 125 in details in the Appendix of *Tosi et al.* (2014). It was originally applied to VIR data acquired at  
 126 Vesta, and subsequently adapted to VIR data acquired at Ceres (Tosi et al., 2018a, 2019a) and to  
 127 Rosetta/VIRTIS data acquired at the comet 67P/Churyumov-Gerasimenko (Tosi et al., 2019b).  
 128 Briefly, a synthetic radiance spectrum is computed by summing the solar contribution and the  
 129 thermal contribution, with emissivity and temperature defined by their respective first guesses. The  
 130 Kirchoff's law is used to relate reflectance with emissivity. This is a two-step process: in the first  
 131 step, spectral emissivity and temperature providing the best fit with the measured spectral radiance  
 132 within the instrumental error in the 4.5–5.1  $\mu\text{m}$  range (where thermal emission is predominant on  
 133 most of the dayside) are iteratively and simultaneously computed in a cycle, until convergence  
 134 around stable values is achieved. In the second step, the scalar value of the surface temperature is  
 135 retained and a second Bayesian retrieval is performed by considering a broader spectral range

136 starting 0.5  $\mu\text{m}$  shortward of the crossover point to compute the spectral emissivity up to the upper  
 137 bound of VIR sensitivity (5.1  $\mu\text{m}$ ). Formal errors on the unknown quantities, related to random  
 138 variations of the signal, are also a standard output of the Bayesian algorithm: each temperature  
 139 image of Ceres can be associated to an image of the formal errors on the retrieved values, and  
 140 similarly, for each wavelength where emissivity is retrieved, there is an associated uncertainty. VIR  
 141 is not sensitive to physical temperatures on the nightside of Ceres, where the signal from the target  
 142 is considerably low. In VIR data acquired at Ceres, uncertainties increase with decreasing surface  
 143 temperature, and 170–180 K is the typical minimum temperature value that can still be retrieved  
 144 while keeping uncertainties  $< 30$  K (typical uncertainties are  $< 1$  K for temperature values  $> 200$  K).

## 145 **2.2 The Thermophysical Model**

146 The determination of the thermal inertia from measured temperatures requires a thermophysical  
 147 model [e.g. *Rozitis et al., 2011, Delbo et al., 2015*]. We have used the one-dimensional model  
 148 described in Capria et al. (2014) and Rognini et al. (2019), that solves the heat conduction equation  
 149 and provides the temperature as a function of thermal conductivity, albedo, emissivity, density, and  
 150 specific heat. The details of the code are reported in the above-mentioned papers; we here briefly  
 151 recall its main points.

152 The model is applied to a detailed shape model of Ceres in order to take into account the  
 153 instantaneous illumination [*Raymond et al., 2011; Preusker et al., 2016*]. The code solves with a  
 154 finite-differences scheme the 1D heat transport equation in all the layers into which the internal  
 155 radius has been subdivided:

$$156 \quad \rho c \frac{\partial T}{\partial t} = \frac{\partial}{\partial x} \left( k \frac{\partial T}{\partial x} \right) \quad (1)$$

157 where  $\rho$  is the density,  $c$  the specific heat,  $T$  the temperature,  $t$  the time,  $x$  the depth and  $k$  is the  
 158 thermal conductivity. The surface boundary condition is:

$$159 \quad \frac{S(1-A)\mu}{r^2} = X\sigma T^4 + k \frac{\partial T}{\partial x} \quad (2)$$

160 where  $S$  is the solar constant,  $A$  is the Bond albedo,  $\mu$  is the cosine of the solar incidence angle,  $r$  is  
 161 the heliocentric distance in AU,  $\sigma$  is the Stefan-Boltzmann constant, and  $X = (1 - \varepsilon\xi)\varepsilon$  is a  
 162 “roughness parameter” where  $\varepsilon$  is the emissivity and  $\xi$  is the sub-pixel roughness.  $\xi$  is a measure of  
 163 the surface irregularity at a scale smaller than the shape model and larger than the thermal skin  
 164 depth; it can be interpreted, for example, as the percentage of cratered terrain with respect to flat  
 165 terrain [Müller and Lagerros, 1998; Keihm et al., 2012]. Flat surfaces will have  $\xi$  values close to 0,  
 166 while very irregular surfaces will have values approaching unity; moreover, high values of  $\xi$  will  
 167 increase the computed surface temperature, while low values will have an opposite effect. We used  
 168 an albedo map that has been calculated by conversion of a reflectance map at 1.2  $\mu\text{m}$  [Ciarniello et  
 169 al., 2017], this being a good proxy for the reflectance at 0.55  $\mu\text{m}$  (the peak of the solar spectrum),  
 170 with differences of a few % [Longobardo et al., 2019]. It should be noted that, while the bolometric  
 171 Bond albedo of Ceres at 0.55  $\mu\text{m}$  is  $0.037 \pm 0.002$  on average [Li et al., 2019], Occator bright spots  
 172 have a Bond albedo rising up to  $0.24 \pm 0.01$  through the Dawn Framing Camera clear filter [Li et  
 173 al., 2016], i.e.  $\sim 6.5$  times the Ceres average.

174 The model is applied to a given location specified by planetocentric coordinates (latitude and  
 175 longitude) referred to a digital shape model of Ceres [Preusker et al., 2016]. The corresponding  
 176 illumination conditions at any step within a given time interval are derived through SPICE-based  
 177 software and navigational databases, the so-called “SPICE kernels” [Acton, 1996], keeping into  
 178 account the position of Ceres along its orbit and that of the Dawn spacecraft. Time interval and  
 179 steps are optimized so as to stabilize the results of the computation.

180 We assume that the surface of Ceres is covered by a layer of particulate material (regolith), ranging  
 181 from very fine dust to incoherent rocky debris, with density increasing with depth. The formulae for  
 182 density and thermal conductivity are based on the properties of the particulate material, which have

183 been derived from ground and spacecraft observations, lunar in-situ measurements and returned  
 184 samples [Capria *et al.*, 2014; Vasavada and Paige, 1999; Vasavada *et al.*, 2012]. Surface density  
 185 ranges from 1200 to 1350 kg/m<sup>3</sup> (fine dust and regolith, respectively, see **Tab. 2**) at the surface and  
 186 increases with depth, while thermal conductivity has the form:

$$187 \quad k(T) = k_{cond} + k_{rad}T^3 \quad (3)$$

188 where  $k_{cond}$  is the conductive term (that takes into account the conductive heat transfer across the  
 189 particles) and  $k_{rad}$  is the radiative term (that takes into account the radiative heat transfer, sensible at  
 190 high temperatures). For  $k_{cond}$  and  $k_{rad}$  we apply the expressions used in Rognini *et al.* (2019),  
 191 where more details can be found. Laboratory experiments show that the thermal conductivity only  
 192 depends on the physical structure of the soil and not on composition [Opeil *et al.*, 2012]. Three  
 193 kinds of particulate material have been assumed in this work: fine dust, dust, fine regolith, with the  
 194 corresponding density profiles (**Tab. 2**). By assuming these materials type, typical total thermal  
 195 conductivity values (**Eq. 3**) range from about 10<sup>-5</sup> to 0.001 W m<sup>-1</sup> K<sup>-1</sup> (for fine dust and fine  
 196 regolith, respectively); the lower value is probably unrealistic for our work, and represents a  
 197 theoretical lower limit in the range we are looking for.

198 The specific heat for the points located inside the faculae has been set to 1060 J kg<sup>-1</sup> K<sup>-1</sup>, which  
 199 corresponds to the specific heat of sodium carbonate, i.e. the main constituent of the bright faculae.  
 200 For the points outside the faculae we used a temperature-dependent specific heat derived from a fit  
 201 of experimental measurements of materials compatible with Ceres surface [Biele *et al.* 2014]:

$$202 \quad c(T) = a_0 + a_1(T - T_0) + a_2(T - T_0)^2 + a_3(T - T_0)^3 \quad (\text{J kg}^{-1} \text{K}^{-1}) \quad (4)$$

203 where  $T_0 = 250$  K,  $a_0 = 633$  J kg<sup>-1</sup> K<sup>-1</sup>,  $a_1 = 2.513$  J kg<sup>-1</sup> K<sup>-2</sup>,  $a_2 = -0.0022$  J kg<sup>-1</sup> K<sup>-3</sup>,  $a_3 =$   
 204  $-2.8 \times 10^{-6}$  J kg<sup>-1</sup> K<sup>-4</sup>.

205 On a real planetary surface, the derivation of thermal inertia is complicated by the presence of  
 206 small-scale surface roughness, which cannot be detected even in the highest resolution optical

207 imagery, but should be taken into account to properly model the measured heat flow. In this regard,  
208 the problem is degenerate to some extent, because different combinations of parameters,  
209 particularly thermal conductivity and surface roughness, in principle might lead to the same value  
210 of thermal inertia.

## 211 **2.2 Derivation of the Thermal Inertia of Cerealia and Vinalia faculae**

212 In order to perform the analysis of the thermal properties of the surface of the Occator faculae we  
213 used the procedure already applied to determine the average thermal inertia of Ceres (see *Rognini et*  
214 *al.*, 2019 for a detailed description), while the VIR data used in this work come from the XM2  
215 mission phase (**Tab. 1**). The areas selected and analyzed are reported in **Fig. 1** and **Fig. 2**: the  
216 magenta square represents the central part of Cerealia facula, while the cyan square and circle  
217 respectively indicate the portion of Occator's floor west of Cerealia facula and the border of the  
218 facula itself (**Tab. 3**).

219 For each VIR pixel, the retrieved temperature value represents the average temperature measured on  
220 a resolution cell defined by the instantaneous ground footprint as observed at a given time. For each  
221 pixel, a complete set of geometric information, including planetocentric latitude and longitude, and  
222 illumination and observation angles, are available. The retrieved temperature values are affected by  
223 the illumination geometry, while our thermophysical code, for each surface element approximated  
224 by a triangular plate ("facet"), calculates the temperature at zero emission angle (i.e, the local  
225 normal to the surface element). To reduce the differences between theoretical and observed  
226 temperature values, we then discarded all VIR observations with an emission angle greater than  
227  $30^\circ$ , and uncertainties associated with retrieved temperature values greater than 5 K. For every  
228 given area, a set of locations (3-5 points) has been selected in such a way as to cover the area as best  
229 as possible, and for every selected location within a given area, we calculated theoretical  
230 temperature profiles by assuming varying pairs of  $k$  and  $\xi$  values. The set of theoretical curves is

231 then compared with the observed temperature data using a chi-square function defined in Rognini et  
 232 al. (2019), that has to be minimized (for every class of material) as a function of  $\xi$ ; a thermal inertia  
 233 value is subsequently derived from thermal conductivity, density and specific heat capacity (Eq. 1).  
 234 This procedure is based on the fundamental hypothesis that, if for given values of the input  
 235 parameters the theoretical temperatures match the measured ones within the associated  
 236 uncertainties, then the input parameters are retained because they are realistic. More precisely,  
 237 because of the degeneration in roughness-thermal inertia, we identify a range of roughness and  
 238 thermal conductivities that are candidate “real” values, as they match the observations.

239

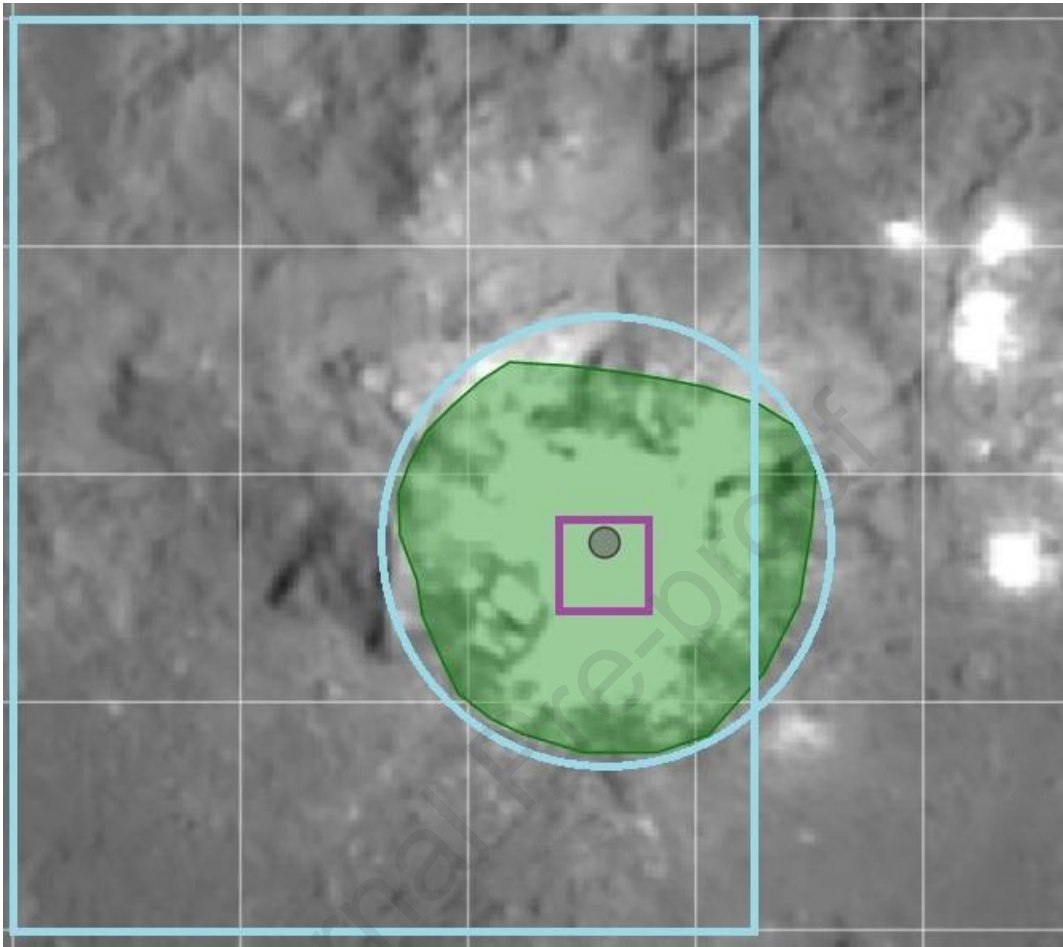
<b>Material</b>	<b>Minimum density (kg/m<sup>3</sup>)</b>	<b>Maximum density (kg/m<sup>3</sup>)</b>
Fine dust	1200	1800
Dust	1320	1930
Fine regolith	1350	1950

240 **Table 2.** Ranges of density values (in kg/m<sup>3</sup>) for the materials considered in this work.

241

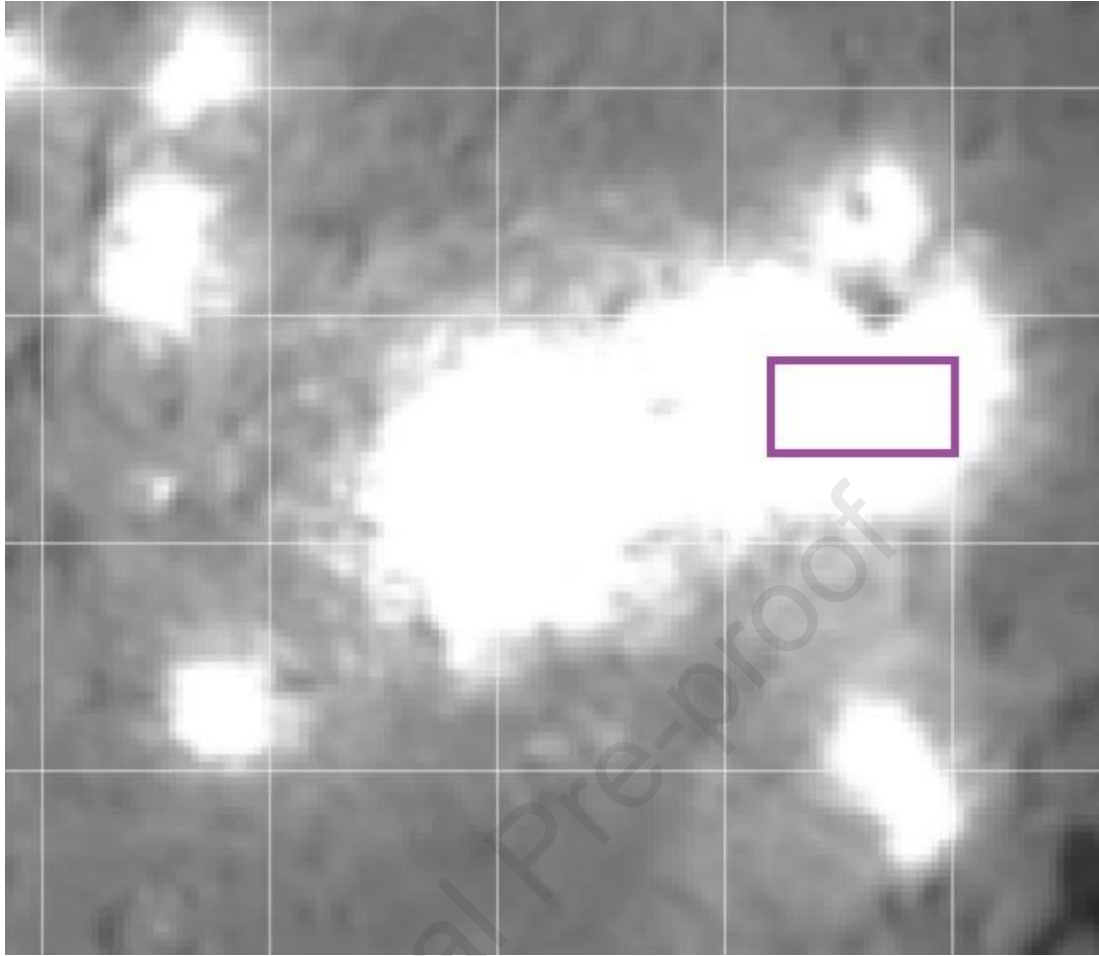
<b>Area</b>	<b>Location (longitude-latitude)</b>
Cerealia	[239.4°, 239.8°] × [19.4°, 19.8°]
Vinalia	[242.6°, 243°] × [20.2°, 20.4°]
Around Cerealia	[237°, 240.5°] × [18°, 22°] (outside the Z area)

242 **Table 3.** The areas considered in this work.  $Z$  is an area defined by  $(lon - 239.6^\circ)^2 + (lat - 19.7)^\circ \leq 1$ .



243

244 **Figure 1.** Selected areas for the Cerealia facula and the the surrounding regions (see **Tab. 3**). The square and circle  
245 drawn in cyan refer to the area selected around Cerealia, while the magenta square identify the area selected in the  
246 central part of Cerealia. The area bordered by the cyan circle and the cyan square is the “Z” area indicated in Tab. 3.



247

248 **Figure 2.** The magenta rectangle surrounds the area selected in Vinalia facula (see **Tab. 3**).

249

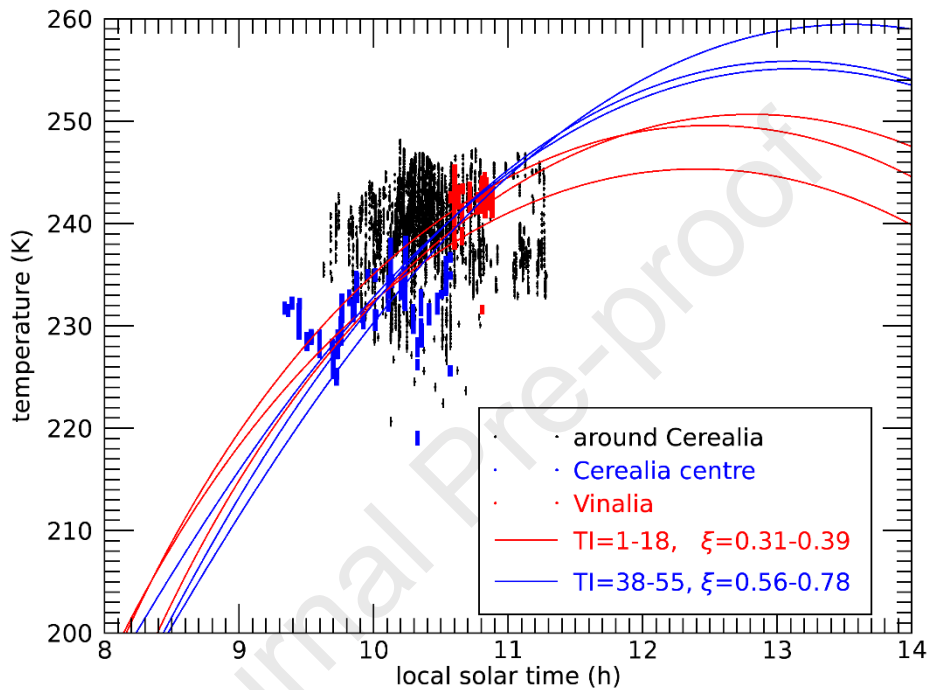
### 250 **3. Results and Discussion**

251 The results of our analysis are summarized in **Fig. 3**, which shows measured data and modeled  
 252 diurnal temperature profiles for the central part of Cerealia, a selected region within Vinalia, and a  
 253 larger area surrounding Cerealia (**Tab. 3**). The temperatures in the central part of Cerealia are lower  
 254 with respect to those in the surrounding regions, while Vinalia facula does not display any thermal  
 255 signature. This could indicate a higher thermal inertia only for the inner region of Cerealia facula. A  
 256 different sub-pixel roughness would also be possible, as explained in subsection **2.2**.

257 Theoretical temperature curves calculated by assuming the material defined as “fine dust”, with  
 258 corresponding thermal inertia up to about  $20 \text{ J m}^{-2} \text{ s}^{-1/2} \text{ K}^{-1}$ , and  $\xi \approx 0.3 - 0.4$ , fit the observations  
 259 of both Cerealia and Vinalia faculae; a similar result is obtained by assuming the material defined as

260 “dust”, with thermal inertia up to  $55 \text{ J m}^{-2} \text{ s}^{-1/2} \text{ K}^{-1}$  and  $\xi \approx 0.6 - 0.8$ . The curves differ between  
 261 them only after 11 h LST, when no observed temperature is available, which precludes the  
 262 possibility to discriminate the most plausible solutions.

263



264

265 **Figure 3.** Comparison between observed (points) and theoretical (lines) temperatures in the areas analyzed in this work.  
 266 The selected areas are reported in **Tab. 3**. For the theoretical temperatures, the corresponding  
 267  $\xi$  values and the resulting thermal inertia are also shown.

268

269 When considering diurnal temperature profiles, the maximum daytime temperature value moves  
 270 from local noon to the local afternoon with increasing thermal inertia, thus the position of this  
 271 maximum in principle could further constrain the thermal inertia value. However, due to operational  
 272 constraints of the Dawn mission, the coverage in terms of local solar time is very limited (typically  
 273 less than 3 hours in the local morning between 9 and 11.5 h LST, see **Fig. 3**), which precludes this  
 274 possibility.

275 Effects of unresolved surface roughness are important in modeling thermophysical properties of  
276 airless bodies. Our model uses the known values of Bond albedo and takes into account the small-  
277 scale surface roughness with a simple  $\xi$  parameter, rather than considering a variable density of  
278 nearly hemispherical concavities at sub-pixel scale, distributed randomly across the surface; the  
279 complexity required to implement this approach in our model goes beyond the scope of the article.

280 To some extent, the thermal conductivity is temperature dependent, and so is the thermal inertia  
281 (**Eq. 1**). When the regolith grains are small, the radiative heat transfer is dominant, particularly at  
282 high temperatures, because the surface contact between grains is small, and the solid-state heat  
283 conduction (transfer by phonons) is less efficient. In this case, the thermal conductivity tends to be  
284 small and is very sensitive to the temperature itself, because the radiative heat transfer is  
285 proportional to  $T^3$ . If the grain size increases then the transfer by phonons becomes dominant, and  
286 the conductivity value increases and is less sensitive to the temperature [Hale & Hapke, 2002].

287 In our previous work [Rognini *et al.*, 2019], we found that the surface temperature of the bright  
288 spots in crater Occator as seen at a resolution of 0.38 km/pixel could be compatible with both low  
289 ( $1-17 \text{ J m}^{-2} \text{ s}^{-1/2} \text{ K}^{-1}$ ) and high (up to about  $140 \text{ J m}^{-2} \text{ s}^{-1/2} \text{ K}^{-1}$ ) thermal inertia. Much higher  
290 resolution VIR data were needed to highlight a temperature difference in Cerealia facula, which  
291 however only shows up in its central part, while Vinalia does not show any thermal contrast at  
292 spatial scales ranging from meters to kilometers. Longobardo *et al.* (2017) found that the phase  
293 curve of the faculae has the same steepness of the average of Ceres despite their larger albedo. They  
294 proposed that this could be due to a mixing of bright and dark material (similar to what happens on  
295 Vesta) or a larger grain size and/or a larger roughness. Cerealia facula could have higher thermal  
296 inertia with respect to the surrounding regions due to its lower temperature; this hypothesis would  
297 agree with the conclusions of Longobardo *et al.* (2017) regarding the larger grain size, because if  
298 the grain size increases then thermal inertia increases. A higher roughness value with respect to  
299 Ceres' average ( $\xi \approx 0.2 - 0.3$ , Rognini *et al.* 2019) is also required in order to fit the temperatures

300 in this area. The Vinalia data could also be fitted by the high thermal inertia curves, but the fact that  
301 no thermal anomaly has been detected in this area suggests that a lower thermal inertia solution,  
302 together with a lower roughness value (magenta curve in the **Fig. 3**), appears to be more likely in  
303 this case. However, spectral unmixing carried out by *Raponi et al. (2017)* suggests that the grain  
304 size of the surface regolith in the faculae could be smaller or anyway compatible with the average  
305 grain size of the surface of Ceres; this conclusion would agree with a low thermal inertia solution,  
306 especially for Vinalia. Anyway, the roughness value required in order to fit the Vinalia temperatures  
307 is higher with respect to the Ceres' average, and this could agree also with the high roughness  
308 values suggested by *Longobardo et al. (2017)*. The high roughness value could be explained by the  
309 young age of Occator: the surface of the faculae has not yet been smoothed because not enough  
310 time has passed, and some surface irregularity could still be present today. Moreover, the brines that  
311 have reached the surface from the interior are not evenly distributed. *Nathues et al. (2017)* have  
312 found that Occator's bright dome formation likely took place over a long period of time, instead  
313 than forming in a single event; this different formation could explain the observed differences  
314 between the faculae. Unlike Cerealia facula, Vinalia facula is composed of a mixture of carbonate  
315 and dark materials (*Palomba et al., 2019*); the dark component, with a different composition and  
316 physical structure with respect to the bright one, could be the reason of a thermal inertia more  
317 similar to the average one of the Ceres' surface.

318

## 319 **5. Conclusions**

320 We have analyzed the temperature data of the faculae in the Occator crater by using the new high  
321 resolution VIR data, acquired in the Extended Mission 2 phase (XM2). The central part of the  
322 Cerealia facula displays a thermal anomaly ( $\sim 10$  K above the average) compatible with a higher  
323 thermal inertia with respect to the surrounding regions; lower values of thermal inertia would also  
324 be possible, but because of the temperature anomaly the higher value is the preferred interpretation.  
325 This can be supported by other results that seems to suggest larger grain sizes of the surface

326 regolith. The Vinalia facula does not display a thermal anomaly, and this is consistent with other  
327 studies that could indicate a grain size comparable with the Ceres' surface average. The faculae  
328 have different history formation and bright/dark material ratio, and this could explain the  
329 differences.

330 **Acknowledgments:** The VIR project is funded by the Italian Space Agency (ASI), ASI-INAF  
331 Contract I/004/12/0. VIR was developed under the leadership of the Istituto di Astrofisica e  
332 Planetologia Spaziale (INAF-IAPS), Rome, Italy. The instrument was built by Selex-Galileo,  
333 Florence, Italy. Support of the Dawn Science, Instrument, Operations Teams, as well as of the  
334 Dawn at Vesta Participating Scientist program, is gratefully acknowledged. We also acknowledge  
335 the hard work carried out by Robert Gaskell in providing a detailed shape model that was used in  
336 this work to properly model the data. Dawn data are archived in NASA's Planetary Data System;  
337 VIR spectral data may be obtained at: <https://sbn.psi.edu/pds/resource/dawn/>. The computational  
338 resources used in this research have been supplied by INAF-IAPS through the DataWell project.

### 339 **References**

- 340 Acton, C. H. (1996), Ancillary data services of NASA's Navigation and Ancillary Information  
341 Facility, *Planetary and Space Science*, **44**, 65-70
- 342 Audouard, J., Poulet, F., Vincendon, M., et al. (2014), Mars surface thermal inertia and  
343 heterogeneities from OMEGA/MEX, *Icarus*, **233**, 194–213
- 344 Biele, J., Pelivan, I., Kuhrt, E., Davidsson, B., Choukroun, M., Alexander, C. J. (2014),  
345 Recommended values and correlations of thermophysical properties for comet modelling, American  
346 Geophysical Union, Fall Meeting 2014, abstract id.P41C-3915
- 347 Capria, M. T. et al (2014), Vesta surface thermal properties map, *Geophysical Research Letters*, **41**,  
348 1438-1443

- 349 Carrozzo, F. G., de Sanctis, M. C., Raponi, A., Ammannito, E., Castillo-Rogez, J., Ehlmann,  
350 B. L., Marchi, S., Stein, N., Ciarniello, M., Tosi, F., Capaccioni, F., Capria, M. T., Fonte,  
351 S., Formisano, M., Frigeri, A., Giardino, M., Longobardo, A., Magni, G., Palomba, Zambon,  
352 F., Raymond, C. A., & Russell, C. T. (2018). Nature, Formation, and distribution of carbonates  
353 on Ceres. *Science Advances*, **4**(3), e1701645. <https://doi.org/10.1126/sciadv.1701645>
- 354 Ciarniello, M., De Sanctis, M. C., et al. (2017), Spectrophotometric properties of dwarf  
355 planet Ceres from the VIR spectrometer on board the Dawn mission, *Astronomy & Astrophysics*,  
356 **598**, A130
- 357 Delbo, M., and P. Tanga (2008), Thermal inertia of main belt asteroids smaller than 100 km from  
358 IRAS data, *Planet. Space Sci.*, **257**, 259–265
- 359 Delbo, M., Mueller, M., Emery, J. P., Rozitis, B., & Capria, M. T. (2015). Asteroid  
360 thermophysical modeling. In P. Michel, et al. (Eds.), *Asteroids IV*, (pp. 107–128). Tucson: Univ. of  
361 Arizona. DOI: 10.2458/azu\_uapress\_9780816532131-ch006
- 362 De Sanctis, M. C., et al. (2011), The VIR spectrometer, *Space Sci. Rev.*, **163**, 329–360
- 363 De Sanctis, M. C., Raponi, A., Ammannito, E., Ciarniello, M., Toplis, M. J., McSween, H.  
364 Y., Castillo-Rogez, J. C., Ehlmann, B. L., Carrozzo, F. G., Marchi, S., & Tosi, F. (2016).  
365 Bright carbonate deposits as evidence of aqueous alteration on (1) Ceres. *Nature*, **536**(7614), 54–  
366 57. <https://doi.org/10.1038/nature18290>
- 367 Harris, A. W., and J. S. V. Lagerros (2002), Asteroids in the thermal infrared, in *Asteroids III*,  
368 edited by W. F. Bottke et al, pp. 205–218, Univ. of Arizona Press, Tucson, Ariz.
- 369 Jaumann, R., Preusker, F. et al. (2017), Topography and Geomorphology of the Interior of Occator  
370 Crater on Ceres, *EPSC Abstract*, **11**

- 371 Keihm, S. J., et al. (2012), Interpretation of combined infrared, submillimeter, and millimeter  
372 thermal flux data obtained during the Rosetta fly-by of Asteroid (21) Lutetia, *Icarus*, **221**, 395–404
- 373 Li, J.-Y. et al. (2016). Surface albedo and spectral variability of Ceres. *ApJ* **817**, L22, Doi:  
374 10.3847/2041-8205/817/2/L22.
- 375 Li, J.-Y., et al. (2019). Spectrophotometric modeling and mapping of Ceres. *Icarus* **322**, 144-167.  
376 Doi: 10.1016/j.icarus.2018.12.038.
- 377 Longobardo, A. et al. (2017), Photometry of Ceres and Occator faculae as inferred from VIR/Dawn  
378 data, *Icarus*, doi.org/10.1016/j.icarus.2018.02.022
- 379 Longobardo, A., Palomba, E., Carrozzo, F. G., et al. (2017), Mineralogy of the Occator Quadrangle,  
380 *Icarus*, in press, doi: 10.1016/j.icarus.2017.09.022
- 381 Longobardo, A., Palomba, E., Galiano, A., De Sanctis, M.C., Ciarniello, M., Raponi, A., Tosi, F.,  
382 Schröder, S.E., Carrozzo, F.G., Ammannito, E., Zambon, F., Stephan, K., Capria, M.T., Rognini,  
383 E., Raymond, C.A., Russell, C.T. (2019). Photometry of Ceres and Occator faculae as inferred from  
384 VIR/Dawn data, *Icarus*, **320**, 97-109.
- 385 Müller, T. G., and J. S. V. Lagerros (1998), Asteroids as far-infrared photometric standards for  
386 ISOPHOT, *Astron. Astrophys.*, **338**, 340–352
- 387 Nathues, A., Hoffmann, M., Schäfer, M., et al. (2015), Sublimation in bright spots on (1) Ceres,  
388 *Nature*, **528**, 237
- 389 Nathues, A., Hoffmann, M., Platz, T., et al. (2016), FC colour images of dwarf planet Ceres reveal a  
390 complicated geological history, *Planetary and Space Science*, **134**, 122–127
- 391 Nathues, A., Platz, T., et al. (2017), Evolution of Occator Crater on (1) Ceres, *Astronomical*  
392 *Journal*, **153**, 112

- 393 Neugebauer, G., Münch, G., et al. (1971), Mariner 1969 Infrared Radiometer Results: Temperatures  
394 and Thermal Properties of the Martian Surface, *Astronomical Journal*, **76**, 719
- 395 Opeil, C. P., Consolmagno, G. J. Et al. (2012), Stony meteorite thermal properties and their  
396 relationship with meteorite chemical and physical states, *Meteoritics & Planetary Science*, **47**, 319-  
397 329
- 398 Palomba, E., Longobardo, A., de Sanctis, M. C., Stein, N. T., Ehlmann, B., Galiano, A.,  
399 Raponi, A., Ciarniello, M., Ammannito, E., Cloutis, E., Carrozzo, F. G., Capria, M. T.,  
400 Stephan, K., Zambon, F., Tosi, F., Raymond, C. A., & Russell, C. T. (2019), Compositional  
401 differences among Bright Spots on the Ceres surface, *Icarus*, **320**, 202–212.  
402 <https://doi.org/10.1016/j.icarus.2017.09.020>
- 403 Preusker, F., Scholten, F., et al. (2016). Dawn at Ceres — Shape Model and Rotational State. 47th  
404 Lunar and Planetary Science Conference, no. 1903
- 405 Raponi, A., Carrozzo, F. G., Zambon, F., de Sanctis, M. C., Ciarniello, M., Frigeri, A.,  
406 Ammannito, E., Tosi, F., Combe, J. P., Longobardo, A., Palomba, E., Pieters, C. M.,  
407 Raymond, C. A., & Russell, C. T. (2019). Mineralogical mapping of Coniraya quadrangle of the  
408 dwarf planet Ceres. *Icarus*, **318**, 99–110. <https://doi.org/10.1016/j.icarus.2017.10.023>
- 409 Raymond, C. A., et al. (2011), The Dawn topography investigation, *Space Sci. Rev.*, **163**, 487–510
- 410 Rognini, E., et al. (2019), High thermal inertia zones on Ceres from Dawn data, *Journal of*  
411 *Geophysical Research*, in press. Doi: <https://doi.org/10.1029/2018JE005733>
- 412 Rozitis, B., and Green, S. F., 2011, Directional Characteristics of Thermal-Infrared Beaming from  
413 Atmosphereless Planetary Surfaces – A New Thermophysical Model, *Monthly Notices of the Royal*  
414 *Astronomical Society*, **415**, 2042–2062.

- 415 Russell, C. T., Raymond, C. (2011), The Dawn Mission to Vesta and Ceres, *Space Science Reviews*,  
416 **163**, 3-23.
- 417 Schröder, S. E., et al. (2017). Resolved spectrophotometric properties of the Ceres surface from  
418 Dawn Framing Camera images. *Icarus* **288**, 201-225. Doi: 10.1016/j.icarus.2017.01.026.
- 419 Stein, N. T., Ehlmann, B. L., et al. (2017), The formation and evolution of bright spots on Ceres,  
420 *Icarus*, in press, doi: 10.1016/j.icarus.2017.10.014
- 421 Tosi, F. et al. (2014). Thermal measurements of dark and bright surface features on Vesta as derived  
422 from Dawn/VIR, *Icarus*, **240**, 36-57. Doi: 10.1016/j.icarus.2014.03.017.
- 423 Tosi, F. et al. (2018a). Mineralogy and temperature of crater Haulani on Ceres. *Meteorit. Planet.*  
424 *Sci.* **53** (9), 1902-1924. Doi: 10.1111/maps.13078.
- 425 Tosi, F. et al. (2018b). Temperature and emissivity of specific regions of interest on Ceres.  
426 European Planetary Science Congress 2018, held 16-21 September 2018 at TU Berlin, Berlin,  
427 Germany, id.EPSC2018-555.
- 428 Tosi, F. et al. (2019a). Mineralogical analysis of the Ac-H-6 Haulani quadrangle of the dwarf planet  
429 Ceres. *Icarus* **318**, 170-187. Doi: 10.1016/j.icarus.2017.08.012.
- 430 Tosi, F. et al. (2019b). The changing temperature of the nucleus of comet 67P induced by  
431 morphological and seasonal effects, *Nature Astronomy* **3** (7), 649-658. Doi: 10.1038/s41550-019-  
432 0740-0.
- 433
- 434 Vasavada, A. R., Paige, D. A. (1999), Near-Surface Temperatures on Mercury and the Moon and  
435 the Stability of Polar Ice Deposits, *Icarus*, **141**, 173-193.

436 Vasavada, A. R. et al. (2012), Lunar equatorial surface temperatures and regolith properties from  
437 the Diviner Lunar Radiometer Experiment, *Journal of Geophysical Research*, **117**, E00H18.

Journal Pre-proof

- New high resolution data revealed a thermal anomaly in the center of Cerealia facula
- Higher thermal inertia may be an indicator of higher grain size or cementation
- Faculae are not homogeneous, different evolutionary history may be possible

Journal Pre-proof

**Declaration of interests**

The authors declare that they have no known competing financial interests or personal relationships that could have appeared to influence the work reported in this paper.

The authors declare the following financial interests/personal relationships which may be considered as potential competing interests:

Journal Pre-proof